# Activated drying in hydrophobic nanopores and the line tension of water

Ludivine Guillemot, Thierry Biben, Anne Galarneau, Gérard Vigier, Élisabeth Charlaix

# Activated drying in hydrophobic nanopores and the line tension of water

Ludivine Guillemot[a], Thierry Biben[a], Anne Galarneau[b], Gérard Vigier[c], and Élisabeth Charlaix[d,1]

[a]Laboratoire de Physique de la Matière Condensée et Nanostructures, Université Lyon 1, Centre National de la Recherche Scientifique Unité Mixte de Recherche 5586, 69622 Villeurbanne Cedex, France; [b]Institut Charles Gerhardt Montpellier, Unité Mixte de Recherche 5253 Université Montpellier 2, Ecole Nationale Supérieure de Chimie de Montpellier, Université Montpellier 1, 34296 Montpellier Cedex 5, France; [c]Laboratoire Matériaux Ingénierie et Sciences, Institut National des Sciences Appliquées de Lyon, 69621 Villeurbanne Cedex, France; and [d]Laboratoire Interdisciplinaire de Physique, Université Joseph Fourier, Unité Mixte de Recherche 5588, 38402 St. Martin d'Heres, France

Edited by Pablo Gaston Debenedetti, Princeton University, Princeton, NJ, and approved October 4, 2012 (received for review May 6, 2012)

**We study the slow dynamics of water evaporation out of hydrophobic cavities by using model porous silica materials grafted with octylsilanes. The cylindrical pores are monodisperse, with a radius in the range of 1–2 nm. Liquid water penetrates in the nanopores at high pressure and empties the pores when the pressure is lowered. The drying pressure exhibits a logarithmic growth as a function of the driving rate over more than three decades, showing the thermally activated nucleation of vapor bubbles. We find that the slow dynamics and the critical volume of the vapor nucleus are quantitatively described by the classical theory of capillarity without adjustable parameter. However, classical capillarity utterly overestimates the critical bubble energy. We discuss the possible influence of surface heterogeneities, long-range interactions, and high-curvature effects, and we show that a classical theory can describe vapor nucleation provided that a negative line tension is taken into account. The drying pressure then provides a determination of this line tension with much higher precision than currently available methods. We find consistent values of the order of −30 pN in a variety of hydrophobic materials.**

drying transition | hydrophobicity | kinetics | nanobubbles | mesoporous silica

A remarkable property of water is its ability to form nanosize bubbles, or cavities, on hydrophobic bodies (1). Since their first direct observations through atomic force microscopy about a decade ago (2, 3), surface nanobubbles on hydrophobic surfaces have raised considerable interest, and they are believed to play a major role in surface-driven phenomena, such as boundary slippage of water flows, heat transfer at walls, vaporization and boiling, surface cleaning, etc. (4, 5). In a different context, the evaporation of water in the vicinity of hydrophobic bodies has been studied as a core mechanism for the hydrophobic interaction mediated by water (6–8), which plays a central role in biological matter. The formation of cavities able to bridge hydrophobic units provides a driving force for protein folding and supermolecular aggregation (9). Simulation examples of such drying-induced phenomena include the collapse of a polymer chain, multidomain proteins, and hydrophobic particles (9–13).

Despite their direct observation, the easy formation and the high stability of nanobubbles on hydrophobic bodies still raise fundamental questions (5, 14, 15). Because of significant theoretical work, it is now established that, at the scale of the nanometer, macroscopic concepts apply: hydrophobicity is described by interfacial energies, and the drying transition in hydrophobic confinement is a first-order transition triggered by the nucleation of a critical vapor bubble (1). The energy barrier limiting the kinetics of this transition is a strong signature of nanobubbles properties. Evaporation kinetics has also been pointed out as the most direct measure of the importance of hydrophobic collapse in protein folding (9). However, rate effects in the drying transition have not received much attention. A few numerical studies have addressed the rate of evaporation of liquid water confined between hydrophobic plates (16–19). The nucleation barrier has been measured with different methods, and it has been shown to increase strongly with the slit separation. The classical theory of capillarity has been shown to overestimate the numerical findings (17, 18). The classical capillarity is a key framework to understand nucleation phenomena, but it is based on macroscopic considerations and does not include specific features, like fluctuations or line energies that can affect interfaces at nanometric scales. There is, however, no consensus about the leading effect at these scales. Fluctuations are invoked in ref. 18 to explain the observed nucleation barrier reduction, whereas line tension is shown to account for the observed deviations in ref. 19. Experimental studies are scarce, because the rate or time variable is generally ignored in studies of adsorption and desorption of confined liquids.

Here, we use highly ordered nanoporous silicas to study the dynamics of water evaporation in hydrophobic confinement. Micelle-templated silicas (MTSs) have quasi-1D mesopores shaped in the form of cylinders of monodisperse radius adjustable from 1 to 5 nm. These model materials have been used as nanoscale laboratory to study the phase diagram of confined liquids (20, 21). In previous works (22, 23), we used silane-grafted MCM-41 (Mobil Crystalline Material 41) to study water confined by hydrophobic walls. Liquid water penetrates into the nanopores at high pressure, reaching 500 bars for nanometer-sized pores. The intrusion pressure of water in the cylindrical pores scales as the inverse of their radius down to radii of 1.3 nm, according to the Laplace law of capillarity (Eq. **1**):

$$P_{\text{int}} = -\frac{2\gamma_{\text{lv}}\cos\theta}{R_{\text{p}}} = 2\frac{\gamma_{\text{sl}}-\gamma_{\text{sv}}}{R_{\text{p}}}, \qquad [1]$$

with $\gamma_{\text{sl}}$, $\gamma_{\text{sv}}$, and $\gamma_{\text{lv}}$ being the solid/liquid, solid/vapor and liquid/vapor surface tensions, respectively. This intrusion law shows the model character of hydrophobized MTS to provide a geometrically and energetically well-defined confinement. The drying transition is obtained by lowering the pressure. Liquid water becomes metastable and finally, empties the nanopores at a pressure $P_{\text{ext}}$ lower than the intrusion pressure (24). The drying pressure $P_{\text{ext}}$ is not described by the Young–Laplace law (1) and increases with temperature (23). Those features are in good qualitative agreement with a drying triggered by the nucleation of a critical vapor bubble on the pore walls.

Author contributions: G.V. and É.C. designed research; L.G. and T.B. performed research; T.B. and A.G. contributed new reagents/analytic tools; L.G., G.V., and É.C. analyzed data; and É.C. wrote the paper.

The authors declare no conflict of interest.

This article is a PNAS Direct Submission.

[1]To whom correspondence should be addressed. E-mail: elisabeth.Charlaix@ujf-grenoble.fr.

This article contains supporting information online at www.pnas.org/lookup/suppl/doi:10.1073/pnas.1207658109/-/DCSupplemental.

We report here investigations of the drying kinetics of the hydrophobic nanopores. For this study, we have developed a device that allows us to perform intrusion–extrusion cycles at finite rates ranging from 0.1 to 100 $s^{-1}$ (25). The dynamic study allows us to get quantitative access to the volume of the critical vapor bubbles initiating the drying and the energy barrier. Although the volume of the critical bubbles is remarkably well-predicted by the classical theory of capillarity, the latter overestimates considerably the energy barrier for their formation. We show that the low energy barrier observed is a strong support of a negative line tension of water on the silane monolayer. The drying pressure provides a measurement of this line tension, completely independent from other experimental methods and with a much higher precision.

## Results

We use here three different MTSs: MCM-41 (26, 27), SBA-15 (Santa Barbara Amorphous 15) (28, 29), and HMS (Hexagonal Mesoporous Silica) (30, 31), which are all shaped in the form of cylindrical pores with a narrow size distribution. Their synthesis, silanization with octyldimethylsilane, and pore size determination with nitrogen sorption at 77 K are described in *SI Text*, section I. The materials exhibit some differences in their organization and internal pore surface. The pore radii of the grafted materials are 1.34 ± 0.1 nm (MCM-41), 1.54 ± 0.1 nm (HMS), and 2.15 ± 0.25 nm (SBA-15) (Table 1). An instrumented, deformable cell is filled under vacuum with the degassed material and pure water, and water is forced in the pores up to full saturation (Fig. 1). The cell volume $V$ is then increased at a constant rate until water empties the nanopores, and the initial cell volume is recovered. The intrusion and drying transitions appear as quasiplateaus on the pressure-volume (P-V) curves (Fig. 1).

Fig. 2 shows the typical behavior of the drying pressure as a function of the time $t_{ext}$ of the drying process. The latter is defined and measured as the time spent on the drying plateau (Fig. 1). A logarithmic growth is obtained for all of the MTSs at all of the temperatures investigated. In contrast, the intrusion pressure exhibits much smaller kinetic effect.

This logarithmic kinetics is a strong signature of the activated processes that govern the drying transition. We argue that the mechanism limiting the drying process is the nucleation in each pore of a vapor bubble extending across the section and forming

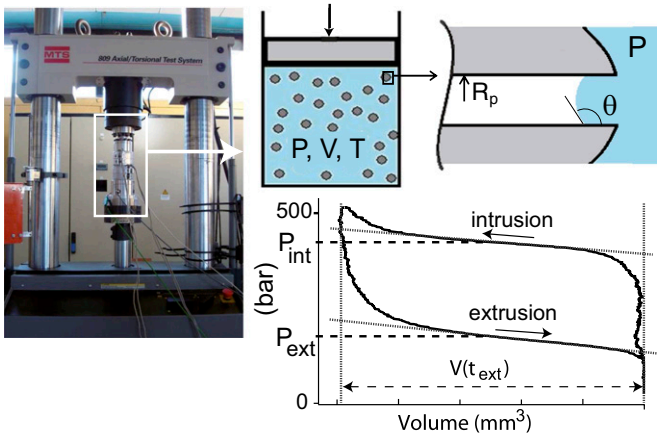


**Fig. 1.** Intrusion/extrusion of water in hydrophobic mesoporous silicas. A thermally regulated cell containing water and the material is placed in a traction machine (*Left*) to measure the pressure–volume isotherms (*Lower Right*). The volume change is driven at a constant velocity in the range of 0.08–80 mm/s. The intrusion and extrusion pressures, $P_{int}$ and $P_{ext}$, respectively, are determined as the average pressure in the corresponding plateaus of the P-V isotherms (24).

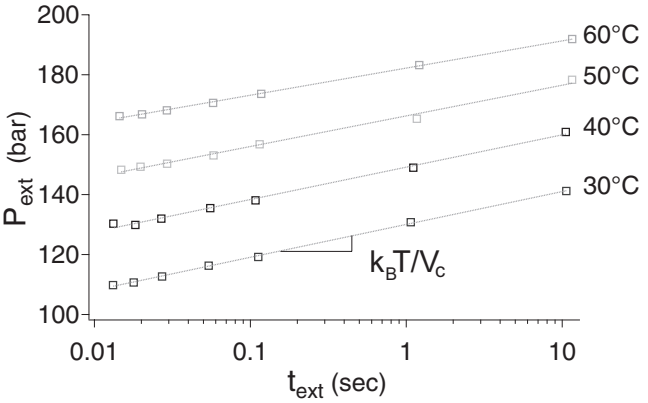


**Fig. 2.** Variation of the extrusion pressure $P_{ext}$ with the logarithm of the time $t_{ext}$ during which extrusion occurs for the MCM-41 material at different temperatures. The other materials show similar logarithmic growth of $P_{ext}$ with $t_{ext}$.

two disconnected menisci (Fig. 3). The drying time, in each independent pore of average length $L$, is then related to the rate of nucleation of a spanning bubble: $I = (\nu L/b)e^{-\Delta\Omega_c/k_BT}$, by $It_{ext} \cong 1$. Here, $\Delta\Omega_c$ is the energy of the critical vapor nucleus, $b$ and $\nu$ are microscopic length scale and frequency, respectively, and $k_BT$ is the thermal energy. This rate leads to a classical nucleation law (Eq. **2**):

$$\Delta\Omega_c = k_BT \ln(L\nu t_{ext}/b). \quad [2]$$

Dimensionally, we expect that $\Delta\Omega_c$ depends on the pressure only through a term $PV_c$ involving the volume of the critical nucleus $V_c$. Hence, the drying pressure should express as (Eq. **3**):

$$P_{ext} = \frac{k_BT}{V_c}\ln\frac{t_{ext}}{t_o} + P^o_{ext}(T), \quad [3]$$

with $P^o_{ext}(T)$ being the extrusion pressure measured at some reference extrusion time $t_o$. If the volume of the vapor nucleus does not depend on the liquid pressure, $P_{ext}$ is expected to grow logarithmically with $t_{ext}$. This result describes our data very well. We get values of $V_c$ from the inverse of the slope of the experimental $P_{ext}$ vs. $\log(t_{ext})$ plots for each material and temperature. We obtain $V_c$ = 10.2 ± 1.5 $nm^3$ for the MCM-41, $V_c$ = 17.8 ± 2.7 $nm^3$ for the HMS, and $V_c$ = 51 ± 17 $nm^3$ for the SBA-15 (Fig. 3). The drying of SBA-15 shows a weaker dynamical behavior than the two others, and therefore, the uncertainty on $V_c$ is much larger.

Because classical capillarity describes successfully the intrusion pressure, we compare $V_c$ to the macroscopic calculation in the work by Lefevre et al. (22) for the nucleation of a bubble in a cylinder. The energy barrier is given within 5% by the approximate expression (Eq. **4**):

$$\Delta\Omega_c \simeq P_L K_1(\theta)R_p^3 + K_2(\theta)\gamma_{lv}R_p^2, \quad [4]$$

where $P_L$ is the liquid pressure, and $K_1$ and $K_2$ are functions of the Young's contact angle $\theta$ (detailed in *SI Text*, section I). Note here that, in contrast to bulk nucleation, the critical volume $V_c = R_p^3K_1(\theta)$ does not depend on the applied pressure. The reason for this lack of dependence is that the formation of two disconnected menisci from a bubble growing at the wall of a cylinder occurs through a capillary instability, which is explained in Fig. 4. The theoretical volume $R_p^3K_1(\theta)$ of the critical nucleus can be calculated by taking the contact angle obtained from the

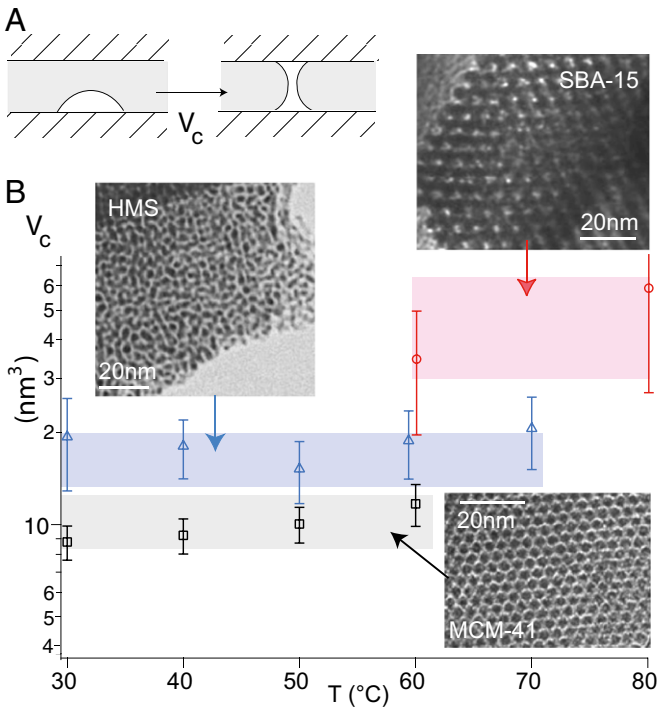


**Fig. 3.** (*A*) Schematic representation of the nucleation process: the critical vapor bubble is able to form two disconnected menisci. (*B*) Nucleus volume $V_c$ measured from the slope of the logarithmic growth of $P_{ext}$ as a function of $t_{ext}$ using Eq. **3** in the three materials at various temperatures. The SBA-15 has a lower extrusion pressure with a smaller slope, leading to a larger uncertainty. The colored rectangles are the theoretical values $K_1(\theta)R_p^3$ calculated using nitrogen sorption pore radii and the contact angle derived from the intrusion pressure (Table 1 and *SI Text*).

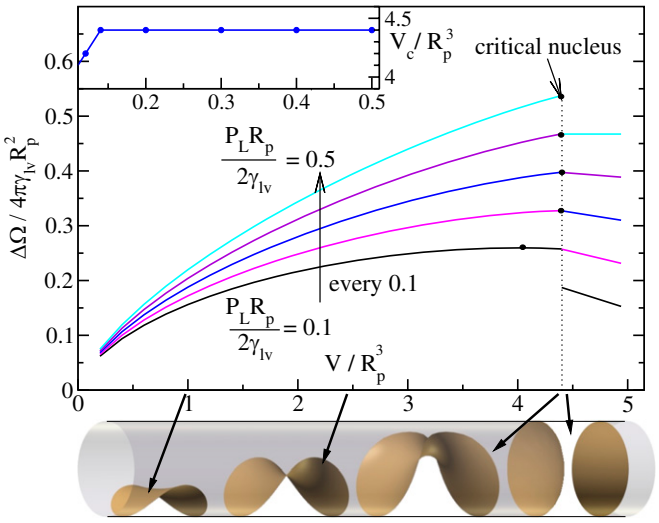


**Fig. 4.** Normalized potential energy $\Delta\Omega/4\pi\gamma_{lv}R_p^2$ of a vapor bubble resting on the wall of a cylinder as a function of its normalized volume $V/R_p^3$. The Young's contact angle is $\theta = 120^o$. The different plots correspond to different values of the liquid pressure $P_L$. The shape of the bubble surface is represented for different volumes. At a critical volume $V_c$, the bubble becomes unstable and spreads over the pore section, forming two disconnected menisci. The maximum value $\Delta\Omega_c$ is equal, or very close, to $\Delta\Omega$ just before instability. (*Inset*) The reduced critical volume $V_c/R_p^3$ as a function of the reduced liquid pressure $P_LR_p/2\gamma_{lv}$.

intrusion pressure (Eq. **1**) as the value of the Young's contact angle $\theta$. Fig. 3 shows its remarkable agreement with the experimental value for the three materials and the different temperatures studied. This agreement is obtained without adjustable parameter: pore radii and their uncertainty are used as derived from the nitrogen sorption isotherms (*Materials and Methods*).

## Discussion

The ability of classical capillarity to describe quantitatively the volume of the critical vapor bubble is remarkable. We should emphasize that we observe here a cavitation process occurring at positive pressures of order of 80–150 bars, whereas usual cavitation in water occurs at strongly negative pressures. This effect is the result of hydrophobic confinement.

However, if classical capillarity predicts, with great precision, the critical bubble volume and the slow dynamics of the drying pressure, it fails by orders of magnitude in predicting the reference pressure (Eq. **5**):

$$P^o_{ext} = \frac{k_BT}{V_c}\ln\frac{L\nu t_o}{b} - \frac{K_2(\theta)}{K_1(\theta)}\frac{\gamma_{lv}}{R_p}. \qquad [5]$$

Assuming a microscopic scale $b \sim$ 1–10 Å and a microscopic frequency $\nu \sim 10^{12}$ to $10^{13}$ s$^{-1}$, Eq. **5** gives a negative value of $P^o_{ext}$ (as low as −200 bars), which is in strong contrast with experimental observation giving $P^o_{ext}$ above 50 bars for all materials and temperatures studied (we have chosen $t_o = 1$ s as the reference time). Put into energy units, the classical model overestimates the nucleation barrier at least by 150 $k_BT$, and is utterly unable to account for the occurrence of cavitation in the hydrophobic mesopores.

Why does the classical theory account so well for the critical bubble volume and so badly for its energy? A major breakdown of classical capillarity at the nucleus scale cannot be invoked. A reduced value of the water surface tension as low as $\gamma_{lv} \sim 40$ mN/m could indeed provide the adequate extrusion pressures. However, such a large deviation from the macroscopic value is consistent with neither the $1/R_p$ scaling of the intrusion pressure found in the MCM-41 nor the state-of-the-art numerical models (32, 33) or capillary forces investigations (34, 35). Actually, the smallest radius of curvature of water menisci reached in our experiments, obtained for MCM-41 intrusion, is of 3.2 nm, not really a molecular value.

Next, one should consider the role of defects able to reduce the energy barrier. Water-repellent defects are needed to favor the vapor phase. However, a close analysis shows inconsistencies with the intrusion process. Chemical defects should have a very large area: taking a maximum value of $\gamma_{lv}$ for the defect dewetting energy $(\gamma_{sl} - \gamma_{sv})_{def}$, which is unrealistically high, the minimum area $A$ providing the needed energy $A\gamma_{lv}(1 + \cos\theta)$, is of the order of 20 nm$^2$ in the MCM-41 and more in the SBA-15 (values of $\theta$ in Table 1). This result corresponds to extended defects covering a significant cylinder portion. Eq. **4** can then be

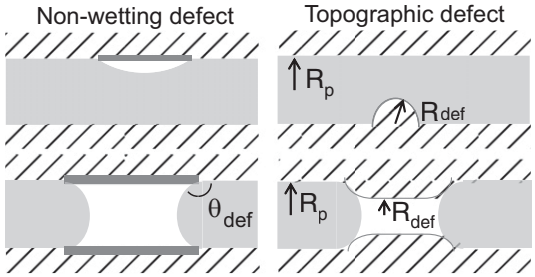


**Fig. 5.** Water repellent defects. (*Upper*) Local defects. (*Lower*) Extended defects.

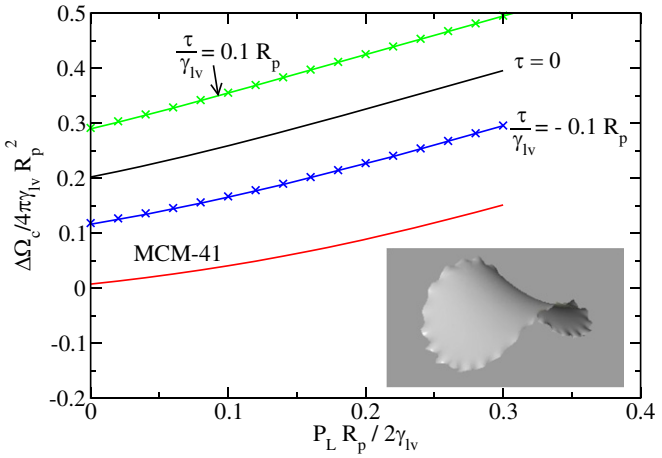


**Fig. 6.** Comparison of two different methods for calculating the normalized energy barrier $\Delta\Omega_c/4\pi\gamma_{lv}R_p^2$ for vapor nucleation in a cylinder. The different colors correspond to different values of the line tension $\tau$. The Young's contact angle is $\theta = 120°$, and the $x$ axis is the normalized liquid pressure. The continuous lines correspond to the first method used in ref. 22, leading to Eq. **6** in the text. The × symbol corresponds to the proper method developed here and described in *SI Text*, section III: the critical nuclei are directly calculated taking into account the finite line tension. The case of MCM41 at 50 °C corresponds to $\tau/\gamma_{lv} = -0.25R_p$ and has been plotted for illustration. The value of the energy barrier at the extruding pressure $P_L$ = 178 bars is 48 $k_BT$. (*Inset*) A nucleus shape for $\tau/\gamma_{lv} = -0.3R_p$.

used to estimate self-consistently the energy barrier on the extended defect, with a local contact angle $\theta_{def}$. Taking the MCM-41 for instance, $[P^o_{ext}(50°C) = 178$ bars$)]$, we need a local contact angle $\theta_{def} \sim 135°$ to provide the adequate barrier. However, the calculated intrusion pressure on such extended defect should be 750 bars, much higher than the maximum pressure around 500 bars reached in the experiment. Such strong defects should not be wetted, and no nucleation should be needed for emptying the pores hosting them (Fig. 5). A similar inconsistency is obtained for topographic defects, such as bumps on the pore walls and pores constrictions (*SI Text*, section II). Thus, the low nucleation barrier shown by the drying pressure cannot be easily attributed to wall defects in the framework of classical capillarity.

Finally, the effect of long-range interactions can be estimated from the value of the disjoining pressure $A_{slv}/6\pi D^3$, where $A_{slv}$ is the wall–vapor–liquid Hamaker constant, and $D$ is the distance of a meniscus portion to the wall. In the heart of the pore, with a typical Hamaker constant of $10^{-20}$ J, the disjoining pressure is of the order of 5 bars, which is not relevant. It is more important close to the contact line. This effect is, indeed, described by the thermodynamic concept of line tension introduced by Gibbs more than a century ago to account for the excess energy caused by long-range interactions close to a three-phases contact line (36, 37). With an expected magnitude of the order $\tau \sim \gamma_{lv}a$ ($a$ being the molecular size, and $\tau \sim 20$ pN for water), line tension plays a significant role only for liquid objects of nanometric size in the three dimensions of space. In contrast to surface tension, it can be negative and thus, reduce the energy of a sessile nanobubble. Experimental determinations of line tension are, however, notoriously difficult, and values reported for water on different substrates vary greatly in amplitude (from $10^{-11}$ to $10^{-6}$ N) and sign and tend to depend on the method used (37, 38). The most direct methods, based on the size dependence of the contact angle of sessile drops/bubbles (39), are limited by the difficulty of exact contact angle measurements at the required scale (1–100 nm) (40) and the bias induced by surface heterogeneities (41). In a previous work, Lefevre et al. (22) attributed the low energy barrier for the drying of silanized MCM-41 to a negative line tension and estimated an amplitude of some $10^{-11}$ N. In their recent numerical study of the evaporation kinetics of water confined between hydrophobic plates, Sharma and Debenedetti (19) also found nucleation energy governed by the line tension but with a positive value. The solid phases are, however, very different in the two cases: the surfaces in ref. 19 are nonsupported 2D solid phases (a single layer of atoms), which should behave quite differently from a 3D solid phase for long-range interactions. In their systematic numerical study of 3D solid and fluid phases interacting with Lennard–Jones potentials, Weijs et al. (42) found a negative line tension for contact angle values between 70° to 130° (42).

We have studied (with a finite element method) the effect of a line tension $\tau$ on the critical nucleus energy. The surprising result is that, although the line tension changes the shape of the critical nucleus, the critical energy is simply given by the expression (22) (Eq. **6**)

$$\Delta\Omega_c \simeq P_L K_1(\theta) R_p^3 + \gamma_{lv} K_2(\theta) R_p^2 + \tau K_3(\theta) R_p, \qquad [6]$$

where $K_1(\theta)$ and $K_2(\theta)$ are the very same functions as in Eq. **4** (case without line tension) and $K_3(\theta)R_p$ is equal to the contact line perimeter of the critical nucleus computed without line tension. This result reflects the almost exact compensation between the line energy gained in changing the shape of the nucleus and the associated losses in volume and surface energies (Figs. 4 and 6).

In contrast to the previous effects, the impact of line tension on the energy barrier is huge: a value of $\tau$ order $\gamma_{lv}a \sim 20$ pN changes the energy barrier by hundreds of $k_BT$ and the drying pressure by hundreds of bars. Thus, we interpret the high value of the drying pressure in the hydrophobic mesopores as a strong support, if not a direct proof, of a negative line tension of water on the C8-silanized silica. The value of the line tension can then be calculated from the experimental values of $P^o_{ext}$ using Eq. **6** and the tabulated values of $K_1$, $K_2$, and $K_3$ given in *Materials and Methods* (Eq. **7**):

$$P^o_{ext} = \frac{k_BT}{V_c}\ln\frac{L\nu t_o}{b} - \frac{K_2(\theta)}{K_1(\theta)}\frac{\gamma_{lv}}{R_p} - \frac{\tau}{R_p^2}\frac{K_3(\theta)}{K_1(\theta)}. \qquad [7]$$

The result is shown in Fig. 7 and Table 1. The precision of ±2 bars on the drying pressure gives a relative precision better than $10^{-2}$ on $\tau$. This is a much higher resolution than the one provided by currently available experimental methods. The values

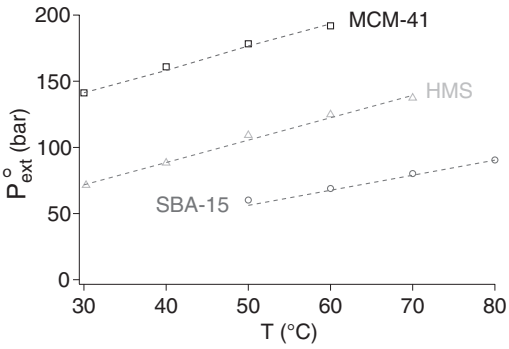


**Fig. 7.** The reference extrusion pressure $P^o_{ext}$ as a function of temperature in the three materials. The dashed line is the best fit obtained by fitting the line tension in Eq. **6**. The pore radii, contact angles, water surface tension, and expressions of $K_1$, $K_2$, and $K_3$ are listed in *SI Text*, section I. In each material, we allow a small linear variation $\tau(T) = \tau_o(1 + \alpha(T - T_o))$. The thermal coefficient $\alpha$ is of the order $-10^{-3}$ K$^{-1}$ (Table 1). For comparison, the thermal coefficient of water surface tension in the same range is $-2.4\ 10^{-3}$ K$^{-1}$.

quoted in Table 1 are calculated using the microscopic quantities $b = 1$ Å, $\nu = 10^{12}$ s$^{-1}$, and $L = 10$ μm. Changing the ratio $b/\nu L$ by a factor 10 or 0.1 changes $\tau$ by less than ±0.6 pN (that is, 1 to 2.5%). The line tension found has consistent values for the three materials ranging from −23 pN in MCM-41 to −35 pN in SBA-15. To account fully for the temperature variation of $P^o_{ext}$, we have allowed a small thermal variation $\tau(T) = \tau_o[1 + \alpha(T - T_o)]$ (Fig. 7 and Table 1). The absolute value $|\alpha|$ of the thermal coefficient is less than $10^{-3}$ K$^{-1}$, to be compared with the thermal coefficient of water surface tension in the same range, −2.4 $10^{-3}$ K$^{-1}$.

The values that we find here are of the same amplitude but opposite sign to the line tension of water measured on hydrophilic surfaces, such as quartz (43) and silica (39). On strongly hydrophobic surfaces, measurements have focused on the shape of nanobubbles. State-of-the-art investigations have not evidenced a variation of the contact angle with the bubble size (40, 44, 45), corresponding to an upper amplitude of about 100 pN for the line tension of water. Therefore, we compare our results with the systematic study by Weijs et al. (42) performed for Lennard-Jones fluids, although the water/silane/silica system investigated here is chemically different. The (negative) line tension is characterized by the ratio of the tension length $l = -\tau/\gamma_{lv}$ to the molecular size $a$. The ratios found here (with $a = 2.7$ Å) are from 1.2 to 1.9, which is in good agreement with thermodynamic expectations and in qualitative agreement with the work by Weijs et al. (42) ($l/a = 0.82$ at contact angle 117°) .

Finally, we find a difference of about −20% (respectively, +20%) for the line tension in MCM-41 (respectively, SBA-15) with respect to HMS. This difference could be because of the topography of the pore walls (SBA-15 is known to have a rougher surface than MCM-41) or a systematic trend with the solid surface curvature, such as described in ref. 46.

## Conclusion

In summary, we have shown here that the drying of water brought into metastable equilibrium inside hydrophobic cavities is a dynamical process with slow logarithmic dynamics. This finding illustrates the importance of carrying out dynamical rate-dependent study of adsorption and desorption phenomena. Such studies are a sensitive probe of the specific mechanisms that control the formation and dynamics of nanobubbles on hydrophobic surfaces. Here, we find that the mechanism that allows one to interpret quantitatively the rate dependence of the extrusion pressure is the thermally activated appearance of a critical vapor nucleus that can be well-described by the macroscopic theory of capillarity, if a negative line tension of water is taken into account. Our approach provides an accurate independent estimate of this line tension, which is consistent with what can be inferred from simulation data or atomic force measurements of droplet shapes. The existence of a negative line tension is an important ingredient for understanding the very high stability of nanobubbles on hydrophobic surfaces and the vaporization of water from repellent cavities, and it has wide implications for heterogeneous cavitation, hydrophobic interactions in biological matter, and more generally, properties of very small liquid objects. Additional work is under progress to study the compressibility of the water/silane hydrophobic interface in the mesopores (47).

**Table 1. Nucleation volume and line tension in the various materials**

| | MCM-41 | SBA-15 | HMS |
|---|---|---|---|
| $R_p$* | 1.34 ± 0.1 | 2.16 ± 0.25 | 1.54 ± 0.1 |
| $\theta_{50°C}$† | 114.8° | 119.1° | 115° |
| $\delta\theta$(°/°C$^{-1}$) | 0.036 | 0.077 | 0.059 |
| $V_c$‡ | 10.2 ± 1.5 | 51 ± 17 | 17.8 ± 2.7 |
| $P^o_{ext}$(50°C)§ | 178 | 60.2* | 109.4 |
| $\tau_{50\ °C}$¶ | −23.3 | −35.5 | −30.1 |
| $\alpha$(°C$^{-1}$) | −1.0 $10^{-3}$ | −0.8 $10^{-3}$ | −0.7 $10^{-3}$ |

*Pore size (nm).
†Intruding contact angle at 50 °C; $\theta(T) = \theta_{50\ °C} + \delta\theta(T - 50)$.
‡Nucleation volume (nm$^3$).
§Reference extrusion pressure at 50 °C (bar; $t_o = 1$ s).
¶Line tension at 50 °C ($10^{-12}$ N); $\tau(T)/\tau_{50\ °C} = 1 + \alpha(T - 50)$.

**Table 2. Other characteristics of the materials**

| | MCM-41 | SBA-15 | HMS |
|---|---|---|---|
| $R_{BJH} - R_{BDB}$ (nm) | 1.25 − 1.43 | 1.91 − 2.40 | 1.44 − 1.64 |
| $R_p$ (nm) | 1.34 ± 0.1 | 2.15 ± 0.25 | 1.54 ± 0.1 |
| $P_{int}$ (50 °C; bar) | 432.1 | 291.1 | 325.5 |
| $\theta_{50\ °C}$ | 114.8° | 119.1° | 115° |
| $\delta\theta$(°/°C$^{-1}$) | 0.036 | 0.077 | 0.059 |
| $K_1(\theta_{50\ °C}) - K_2(\theta_{50\ °C})$ | 4.27 − 3.24 | 4.28 − 2.614 | 4.27 − 3.21 |
| $K_3(\theta_{50\ °C})$ | 12.366 | 12.422 | 12.37 |

## Materials and Methods

The MCM-41 was synthesized from the structuring agent octadecyltrimethylammonium bromide ($C_{18}NMe_3Br$) as described in ref. 27. MCM-41 is a model material presenting independent cylindrical pores that are hexagonally ordered and have a smooth internal surface. SBA-15 was synthesized from the triblock copolymer poly(ethylene oxide)-poly(propylene oxide)-poly(ethylene oxide) $EO_{20}PO_{70}EO_{20}$ as a structuring agent under acidic medium at 60 °C for 24 h (29). SBA-15 also has a hexagonal arrangement of cylindrical pores, but depending on the synthesis temperature, these mesopores can be connected by a secondary network of smaller micropores. We chose a temperature of 60 °C, which prevents the micropores from growing and creating interconnections (29). The HMS was prepared with $C_{16}NH_2$ as the structuring agent, with a ratio $EtOH/H_2O = 0.19$ at an ambient temperature for 24 h (31). The HMS has a smooth internal surface but is less ordered than MCM-41, and the pore network can be randomly connected in few locations. The three mesoporous silicas are silanized by grafting chlorodimethyloctylsilane as described in ref. 48. Before and after silanization, the MTS was characterized by nitrogen adsorption at 77 K (49). The pore size determination was done using two methods: the Barret–Joyner–Halenda method (50), which is classically used but has been shown to underestimate the pore size of hydrophilic silica (49), and the Broekhoff–de Boer method. The pore size of the hydrophobic materials is taken as the average of the two results $R_p = (R_{BdB} + R_{BJH})/2$, and the uncertainty is taken as their difference $\Delta R_p = (R_{BdB} - R_{BJH})/2$. The values are gathered in Table 2.

The experimental device, cell preparation, and obtention of the P-V isotherms of water in the hydrophobic materials are detailed in ref. 25. The intrusion (respectively, drying) pressure is defined as the average pressure value on the corresponding plateau. The intrusion pressure depends weakly on the intrusion rate, and we use quasistatic values obtained at a rate of 0.1 s$^{-1}$. It also depends very weakly on temperature, because $P_{int} = P_{int}(T_o) + \Delta P_{int,T}(T - T_o)$. The Young contact angle derived from Eq. **1** also changes with temperature, because $\theta = \theta(T_o) + \delta\theta(T - T_o)$. Values for the three materials are summarized in Table 2.

In the data analysis, we use the following expressions to interpolate the functions $K_1$, $K_2$, and $K_3$ with $90° \le \theta \le 135°$:

$$K_1(\theta) = 4.1661 + 0.11242 \times \sin(0.11819 \times \theta + 0.16478),$$

$$K_2(\theta) = 20.32 - 0.14879 \times \theta, \text{ and}$$

$$K_3(\theta) = 3.355 + 0.14136 \times \theta - 0.00054762 \times \theta^2.$$

The theoretical calculation of the shape and energy of a vapor bubble in a cylinder in the presence of a line tension is performed with a finite element method and a relaxation algorithm.

**ACKNOWLEDGMENTS.** We thank Thierry Abensur and the European Aeronautic Defence and Space-Astrium Space Transportation Companies for supporting this research.

1. Lum K, Chandler D, Weeks JD (1999) Hydrophobicity at small and large length scales. *J Phys Chem B* 103(22):4570–4577.
2. Ishida N, Inoue T, Miyahara M, Higashitani K (2000) Nano bubbles on a hydrophobic surface in water observed by tapping-mode atomic force microscopy. *Langmuir* 16(16):6277–6380.
3. Tyrrell JW, Attard P (2001) Images of nanobubbles on hydrophobic surfaces and their interactions. *Phys Rev Lett* 87(17):176104.
4. Meyer EE, Rosenberg KJ, Israelachvili JN (2006) Recent progress in understanding hydrophobic interactions. *Proc Natl Acad Sci USA* 103(43):15739–15746.
5. Seddon JRT, Lohse D (2011) Nanobubbles and micropancakes: Gaseous domains on immersed substrates. *J Phys Condens Matter* 23(13):133001.
6. Christenson HK, Claesson PM (2001) Direct measurements of the force between hydrophobic surfaces in water. *Adv Colloid Interface Sci* 91(3):391–436.
7. Chandler D (2002) Hydrophobicity: Two faces of water. *Nature* 417(6888):491.
8. Berne BJ, Weeks JD, Zhou R (2009) Dewetting and hydrophobic interaction in physical and biological systems. *Annu Rev Phys Chem* 60:85–103.
9. ten Wolde PR, Chandler D (2002) Drying-induced hydrophobic polymer collapse. *Proc Natl Acad Sci USA* 99(10):6539–6543.
10. Patel AJ, et al. (2011) Extended surfaces modulate hydrophobic interactions of neighboring solutes. *Proc Natl Acad Sci USA* 108(43):17678–17683.
11. Zhou R, Huang X, Margulis CJ, Berne BJ (2004) Hydrophobic collapse in multidomain protein folding. *Science* 305(5690):1605–1609.
12. Giovambattista N, Lopez CF, Rossky PJ, Debenedetti PG (2008) Hydrophobicity of protein surfaces: Separating geometry from chemistry. *Proc Natl Acad Sci USA* 105(7): 2274–2279.
13. Mittal J, Hummer G (2008) Static and dynamic correlations in water at hydrophobic interfaces. *Proc Natl Acad Sci USA* 105(51):20130–20135.
14. Borkent BM, Dammer SM, Schönherr H, Vancso GJ, Lohse D (2007) Superstability of surface nanobubbles. *Phys Rev Lett* 98(20):204502.
15. Ducker WA (2009) Contact angle and stability of interfacial nanobubbles. *Langmuir* 25(16):8907–8910.
16. Bolhuis PG, Chandler D (2000) Transition path sampling of cavitation between molecular scale solvophobic surfaces. *J Chem Phys* 113(18):8154–8160.
17. Leung K, Luzar A, Bratko D (2003) Dynamics of capillary drying in water. *Phys Rev Lett* 90(6):065502.
18. Luzar A (2004) Activation barrier scaling for the spontaneous evaporation of confined water. *J Phys Chem B* 108(51):19859–19866.
19. Sharma S, Debenedetti PG (2012) Evaporation rate of water in hydrophobic confinement. *Proc Natl Acad Sci USA* 109(12):4365–4370.
20. Liu D, et al. (2007) Observation of the density minimum in deeply supercooled confined water. *Proc Natl Acad Sci USA* 104(23):9570–9574.
21. Zhang Y, et al. (2011) Density hysteresis of heavy water confined in a nanoporous silica matrix. *Proc Natl Acad Sci USA* 108(30):12206–12211.
22. Lefevre B, et al. (2004) Intrusion and extrusion of water in hydrophobic mesopores. *J Chem Phys* 120(10):4927–4938.
23. Lefevre B, et al. (2004) Intrusion and extrusion of water in highly hydrophobic mesoporous materials: Effect of the pore texture. *Coll and Surf A* Physicochem Eng Asp 241:265–272.
24. Eroshenko VA, Regis RC, Soulard M, Patarin J (2001) Energetics: A new field of applications for hydrophobic zeolites. *J Am Chem Soc* 123(33):8129–8130.
25. Guillemot L, Galarneau A, Vigier G, Abensur T, Charlaix E (2012) New device to measure dynamic intrusion/extrusion cycles of lyophobic heterogeneous systems. *Rev Sci Instrum* 83(10):105105.
26. Kresge CT, Leonowicz ME, Roth WJ, Vartuli JC, Beck JS (1992) Ordered mesoporous molecular sieves synthesized by a liquid-crystal template mechanism. *Nature* 359: 710–712.
27. Martin T, Galarneau A, Di Renzo F, Brunel D, Fajula F (2004) Great improvement of chromatographic performance using MCM-41 spheres as stationary phase in HPLC. *Chem Mater* 16(9):1725–1731.
28. Zhao D, et al. (1998) Triblock copolymer syntheses of mesoporous silica with periodic 50 to 300 angstrom pores. *Science* 279(5350):548–552.
29. Galarneau A, et al. (2003) Microporosity and connections between pores in SBA-15 mesostructured silicas as a function of the temperature of synthesis. *New J Chem* 27 (1):73–79.
30. Tanev PT, Pinnavaia TJ (1996) Mesoporous silica molecular sieves prepared by ionic and neutral surfactant templating: A comparison of physical properties. *Chem Mater* 8(8):2068–2079.
31. Di Renzo F, et al. (1999) Textural control of micelle-templated mesoporous silicates: The effects of co-surfactants and alkalinity. *Microporous Mesoporous Mater* 28(3): 437–446.
32. Huang DM, Geissler PL, Chandler D (2001) Scaling of hydrophobic solvation free energies. *J Phys Chem B* 105(28):6704–6709.
33. Dzubiella J, Swanson JMJ, McCammon JA (2006) Coupling hydrophobicity, dispersion, and electrostatics in continuum solvent models. *Phys Rev Lett* 96(8):087802.
34. Fisher LR, Israelachvili JN (1981) Direct measurement of the effect of meniscus force on adhesion: A study of the applicability of macroscopic thermodynamis to microscopic liquid interfaces. *Colloids Surf* 3(4):303–319.
35. Christenson HK (1988) Adhesion between surfaces in undersaturated vapors - A reexamination of the influence of meniscus curvature and surface forces. *J Colloid Interface Sci* 121(1):170–178.
36. Gibbs JW (1957) *The Scientific Papers* (Dover, New York), Vol I.
37. Drelich J (1996) The significance and magnitude of the line tension in three-phase (solid-liquid-fluid) systems. *Colloids Surf A Physicochem Eng Asp* 116:43–54.
38. Amirfazli A, Neumann AW (2004) Status of the three-phase line tension: A review. *Adv Colloid Interface Sci* 110(3):121–141.
39. Pompe T, Herminghaus S (2000) Three-phase contact line energetics from nanoscale liquid surface topographies. *Phys Rev Lett* 85(9):1930–1933.
40. Borkent BM, de Beer S, Mugele F, Lohse D (2010) On the shape of surface nanobubbles. *Langmuir* 26(1):260–268.
41. Checco A, Guenoun P, Daillant J (2003) Nonlinear dependence of the contact angle of nanodroplets on contact line curvature. *Phys Rev Lett* 91(18):186101.
42. Weijs JH, Marchand A, Andreotti B, Lohse D, Snoeijer JH (2011) Origin of line tension for a lennard-jones nanodroplet. *Phys Fluids* 23(2):022001.
43. Zorin Z, Platikanov D, Kolarov T (1987) The transition region between aqueous wetting films on quartz and the adjacent meniscus. *Colloids Surf* 22:147–159.
44. Zhang XH, Maeda N, Craig VSJ (2006) Physical properties of nanobubbles on hydrophobic surfaces in water and aqueous solutions. *Langmuir* 22(11):5025–5035.
45. Zhang XH, Quinn A, Ducker WA (2008) Nanobubbles at the interface between water and a hydrophobic solid. *Langmuir* 24(9):4756–4764.
46. Bauer C, Dietrich S (2000) Shapes, contact angles, and line tensions of droplets on cylinders. *Phys Rev E Stat Phys Plasmas Fluids Relat Interdiscip Topics* 62(2):2428–2438.
47. Sarupria S, Garde S (2009) Quantifying water density fluctuations and compressibility of hydration shells of hydrophobic solutes and proteins. *Phys Rev Lett* 103(3):037803.
48. Martin T, et al. (2001) Towards total hydrophobisation of MCM-41 type silica surface. *Stud Surf Sci Catal* 135:4621–4628.
49. Galarneau A, Desplantier D, Dutartre R, Di Renzo F (1999) Micelle-templated silicates as a test-bed for methods of mesopore size evaluation. *Microporous Mesoporous Mater* 27:297–308.
50. Barrett EP, Joyner LG, Halenda PP (1951) The determination of pore volume and area distributions in porous substances. I. Computations from nitrogen isotherms. *J Am Chem Soc* 73(1):373–380.